



Article

Investigating the Effect of Cross-Conjugation Patterns on the Optoelectronic Properties of 7,7'-Isoindigo-Based Materials

Shiwei Ren ^{1,2,*} , Amirhossein Habibi ³, Yujie Wang ⁴ and Abderrahim Yassar ^{3,*} 

¹ Zhuhai Fudan Innovation Research Institute, Guangdong-Macao Cooperation Zone in Hengqin, Zhuhai 519001, China

² Laboratory of Molecular Materials and Devices, Department of Materials Science, Fudan University, Shanghai 200433, China

³ Laboratory of Physics of Interfaces and Thin Films—CNRS, Ecole Polytechnique, Institut Polytechnique de Paris, Route de Saclay, 91128 Palaiseau, France; amirhossein.habibi@polytechnique.edu

⁴ School of Luoyang Foreign Language, Luoyang 471000, China; wangyujie.chemistry@gmail.com

* Correspondence: shiwei_ren@fudan.edu.cn (S.R.); abderrahim.yassar@polytechnique.edu (A.Y.)

Abstract: Isoindigo (IID) is widely used as a building block for the fabrication of organic semiconductor devices. Understanding the impact of cross-conjugation and linear conjugation on the optoelectronic properties of disubstituted IID is of great importance for the design of improved materials. In this study, phenyl and thienyl groups were substituted at the cross-conjugated 7,7' position of IID to generate three novel organic semiconductor structures with a donor–acceptor architecture. The optoelectronic properties of this IID derivative were investigated and compared with those of the 6,6' linearly conjugated IID analogs using UV–Vis spectroscopy and cyclic voltammetry. The experimental results were compared using density functional theory calculations to provide structure–property relationships based on substitution types and attachment sites for IID. The frontier orbital energy levels of the material did not vary dramatically with the position of the substituent, while the type of substituent showed a more significant influence on the HOMO's energy level and oscillator strength. Phenyl-disubstituted 7,7' IID (7Ph7'Ph) and thienyl-disubstituted 7,7' IID (7Th7'Th) materials were used as electron transport layers in perovskite solar cells with a power conversion efficiency of 5.70% and 6.07%, respectively. These observations enhance our understanding of the electronic structure and optoelectronic properties of IID, guiding the design of the next generation of IID-based semiconductors.

Keywords: cross-conjugation; UV–Vis spectroscopy; DFT calculations; optoelectronic properties; electron transport layers; perovskite solar cells



Citation: Ren, S.; Habibi, A.; Wang, Y.; Yassar, A. Investigating the Effect of Cross-Conjugation Patterns on the Optoelectronic Properties of 7,7'-Isoindigo-Based Materials. *Electronics* **2023**, *12*, 3313. <https://doi.org/10.3390/electronics12153313>

Academic Editor: Mingxing Du

Received: 17 July 2023

Revised: 27 July 2023

Accepted: 31 July 2023

Published: 2 August 2023



Copyright: © 2023 by the authors. Licensee MDPI, Basel, Switzerland. This article is an open access article distributed under the terms and conditions of the Creative Commons Attribution (CC BY) license (<https://creativecommons.org/licenses/by/4.0/>).

1. Introduction

Isoindigo (IID) is an electron-deficient building block that has been intensely developed in organic solar cells and organic field-effect transistor applications. For instance, donor–acceptor conjugated polymers based on IID derivatives showed hole and electron mobilities of up to 14.40 and 16.07 cm² V^{−1} s^{−1}, respectively [1,2]. The power conversion efficiencies of solar cells based on IID–polymer solar cells and IID small molecules exceed 10% and 8%, respectively [3,4]. Furthermore, various IID-based polymers have been used for other applications, such as chemical sensors, organic electrochemical transistors, organic phototransistors, organic thermoelectric generators, etc. [5–9]. There are many reviews of IID analogs for numerous optoelectronic applications [10–15]. As shown on the left side of Figure 1, IID can be structurally tuned to achieve the desired properties. The functionalization of the phenyl ring of IID permits access to various structural modification possibilities, including replacing the phenyl ring with an aromatic heterocycle, extending the conjugation length on the periphery of the phenyl ring, and substituting it with different groups. These methods not only change the molecular planarity but also modulate the

electronic structures. In addition, the modification of nitrogen atoms using different side chains endows materials with different solubility and packing motifs.

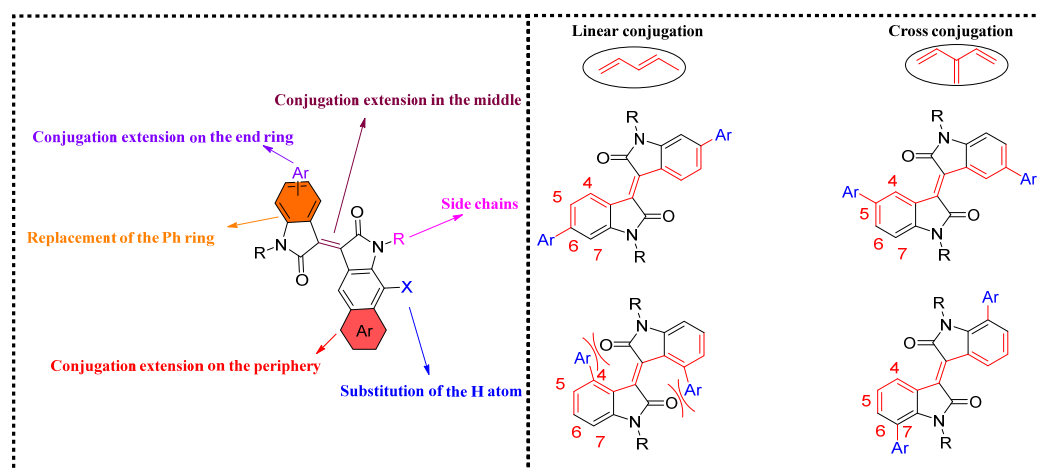


Figure 1. Left: functionalization strategy of IID derivatives; right: effect of substitution of two linking modes for IID-based conjugated derivatives.

Regarding the substitution pattern on the phenyl ring, there are four positions available for introducing functional groups: the 4,4', 5,5', 6,6', and 7,7' positions (Figure 1 right). The 4,4' substitution is restricted due to the unfavorable steric hindrance between the substituent and carbonyl group. The 6,6' substitution results in linearly conjugated chromophores, while 5,5' and 7,7' generate cross-conjugated materials [16]. Broadly speaking, the substitution at the 6,6' position results in the occurrence of conjugation throughout the entire molecule, allowing for more extended π -electron delocalization. Cross-conjugation is defined as the conjugation between two unsaturated π segments that, although not conjugated to each other, are conjugated to an intervening unsaturated segment. Playing with the linkage patterns is an important factor in molecular packing, which governs molecular topology and carrier transport. Materials based on the 6,6' position have been intensively studied, while research into cross-conjugated materials has become increasingly important and urgent [16–18].

2. Materials and Methods

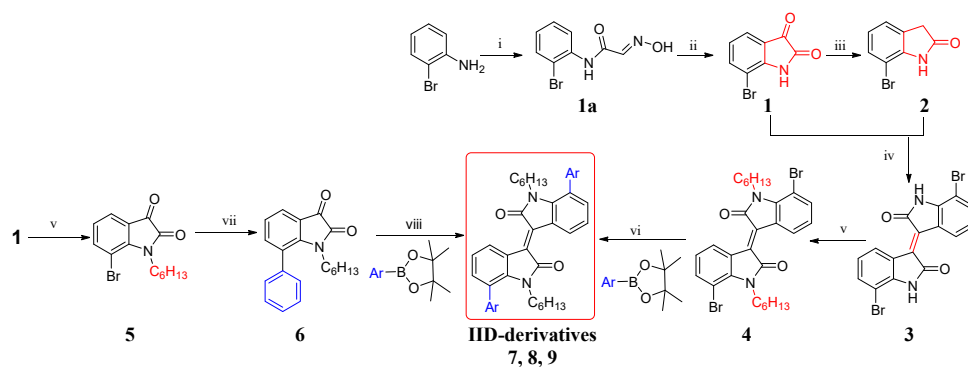
Chemical reagents were purchased from Aldrich and used as received. Solvents were dried and purified using standard techniques. Reactions with air-sensitive materials were carried out using argon. Nuclear magnetic resonance spectra were recorded on a Bruker DMX-300 (300 MHz) spectrometer. Deuterated chloroform was used as the solvent. ^1H NMR chemical shifts were referenced relative to internal tetramethylsilane. The splitting patterns were designated as follows: s (singlet); d (doublet); t (triplet); and m (multiplet). Mass spectrometry was performed using the “Fédération de Recherche” ICOA/CBM (FR2708) platform of Orléans in France. High-resolution mass spectra were carried out using either maXis Q-TOF or Tims TOF (Bruker, Paris, France) in positive ion mode using electrospray ionization (ESI) for the analysis of samples. The analytes were dissolved in a suitable solvent at a concentration of 1 mg/mL and diluted 500 times in methanol (≈ 2 ng/mL). The diluted solutions (2 μL) were delivered to the ionization source via an Ultimate 3000 RSLC chain or Elute UHPLC module in flow injection analysis mode at a flow rate of 100 $\mu\text{L}/\text{min}$ and a mixture of $\text{CH}_3\text{CN}/\text{H}_2\text{O} + 0.1\%$ HCO_2H . The ESI conditions were as follows: capillary and end-plate voltages were set at 4.5 kV and 0.5 kV, respectively; nitrogen was used as nebulizing and drying gas at 0.6 bar and 7.0 L/min^{-1} , respectively, at a drying temperature of 220 $^\circ\text{C}$. UV–Vis spectra were recorded on a Varian Cary model 500 UV–Vis–NIR spectrophotometer using standard quartz cells of 1 cm width and solvents of spectroscopic grade. Electrochemical measurements were carried out

in a dichloromethane solution with tetrabutylammonium perchlorate using a Metrohm Autolab PGSTAT12 Potentiostat. The Ag/AgCl reference electrode was calibrated using a ferrocene/ferrocenium redox couple as an external standard, and it was located at 0.53 V vs. the Ag/AgCl electrode. The oxidation potential was set at -4.80 eV with respect to zero vacuum levels. DFT calculations were performed using the B3LYP/6-311(d, p) basis set of the Gaussian 16 program.

3. Results

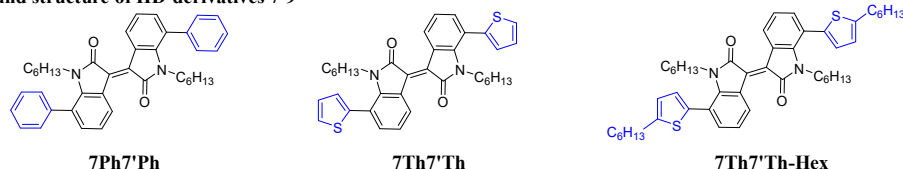
3.1. Synthesis

The 7,7' IID-based materials were synthesized following the procedures summarized in Scheme 1. Commercially available 2-bromoaniline was employed as a precursor to obtain 7-bromoisatin, **1**, via a two-step reaction involving the reaction of chloral hydrate and hydroxylamine. Intermediate **1a** was subsequently electrophilically cyclized in the presence of concentrated sulfuric acid. Hydrazine hydrate was used to reduce **1** to **2**, and then an acid-catalyzed aldol condensation of **1** with **2** was conducted to obtain **3** at an 85% yield. The strong π - π interaction and hydrogen bonding of IID resulted in a poor solubility of **3** in common organic solvents. The hexyl chain was introduced into the two nitrogen atoms of the lactam to obtain **4** at a 90% yield using potassium carbonate as a base. The Suzuki reaction was employed to prepare compounds **7-9** at a sufficiently high yield using $\text{Pd}_2(\text{dba})_3$ as a catalyst, K_3PO_4 as a base, and $\text{P}(\text{o-tyl})_3$ as a ligand. In contrast to **8**, **9** was further introduced with another alkyl chain on the thiophene ring, which was considered a method to further enhance the solubility of the material. An alternative solution to the solubility problem was to use pre-alkylate **1** and subsequently introduce phenyl into **5** via Suzuki coupling to obtain intermediate **6**. Finally, Lawesson's reagent was successfully used to generate **7** at an 82% yield. These compounds with donor-acceptor architecture exhibited good solubility in common organic solvents, such as tetrahydrofuran, dichloromethane, and chlorobenzene. The synthetic procedures and characterizations are described in detail in Supporting Information.



^aReagent and condition: (i) chloral hydrate, Na_2SO_4 , $\text{H}_2\text{NOH}\cdot\text{HCl}$; (ii) H_2SO_4 , 46% over two steps; (iii) $\text{NH}_2\text{NH}_2 \cdot \text{H}_2\text{O}$, reflux, $\text{CH}_3\text{CH}_2\text{ONa}$, Ethanol, 67%; (iv) HCl , AcOH , reflux, 85%; (v) K_2CO_3 , 1-bromohexane, DMF, reflux, 90%; (vi) $\text{Pd}_2(\text{dba})_3$, $\text{P}(\text{o-tyl})_3$, K_3PO_4 , Toluene, H_2O , 65%-85%; (vii) KF , $\text{Pd}(\text{OAc})_2$, MeOH, 67%; (viii) Lawesson's reagent, Toluene, reflux, 82%.

Compound structure of IID-derivatives 7-9



Scheme 1. Synthesis of IID derivatives **7-9**: 7Ph7'Ph, 7Th7'Th, and 7Th7'Th-Hex.

3.2. Crystal Structure and Molecular Packing

The single crystals of **4** and **7** were obtained via slow solvent evaporation from a solvent mixture of dichloromethane and methanol. The crystal structures of these compounds are shown below (Figure 2). The 7,7' IID geometry obtained using X-ray diffraction showed

a planar and trans configuration. The two lactam blocks were almost in the same plane, and the dihedral angle between the phenyl and the lactam plane was 65.61° . A similar phenomenon was observed for IID substituted at the 6,6' position when the phenyl ring was used as a substituent, exhibiting a dihedral angle of 39.20° between the phenyl and the lactam [16]. Molecules **4** and **7** were stacked into a two-dimensional slipped π stacking with distances of 3.43 Å and 3.54 Å, respectively (Figures S1 and S2). The complexation energies of **4** and **7** were theoretically calculated to be 28.99 and 26.17 kcal/mole, respectively. The intermolecular interactions were strong and favorable for efficient charge transport [19]. The resulting structures reported in this paper have been deposited at the Cambridge Crystallographic Data Centre as a supplementary publication (CDCC 2278123–2278124).

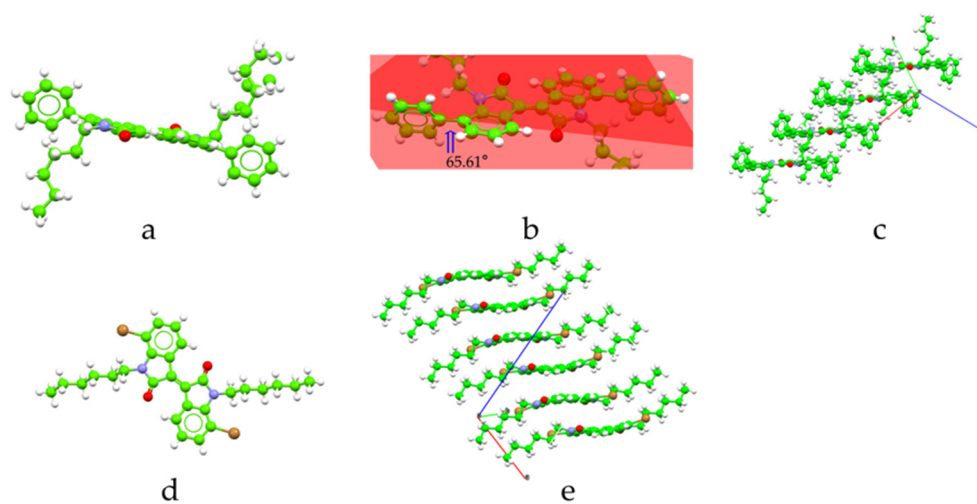


Figure 2. (a): ORTEP representation of compound **7**; (b) the torsion angle between the phenyl group and the lactam plane of **7**; (c) molecular packing of **7** in the solid state; (d) ORTEP representation of compound **4**; (e) molecular packing of compound **4** in the solid state.

3.3. Density Functional Theory Calculations

In attempt to gain insight into how cross-conjugation affects the optoelectronic properties of IID derivatives, their optimized molecular geometries, molar absorption coefficient (ϵ), highest occupied molecular orbital (HOMO) distribution, lowest occupied molecular orbital (LUMO), energy gap (ΔE_c), and oscillator strength (f_{osc}) were calculated using DFT at the B3LYP/6-311 (d, p) level basis [20,21] set of the Gaussian 16 program in order to obtain a low-energy conformation [22,23]. To compare the effects of alkyl chains on the thiophene ring, all long hexyl alkyl chains were retained during the calculations. Figure 3 displays the LUMO and HOMO distributions. It can be clearly observed that the LUMO was mainly distributed on IID units, while the HOMO was delocalized along the backbone. The detailed data of the frontier molecular orbital energies, ϵ , and f_{osc} are shown in Table 1. For the sake of comparison, the results of the DFT calculations with respect to the introduction of phenyl and thienyl at positions 5, 6, and 7—corresponding to reference numbers 5Ph5'/Ph, 5Th5'/Th, 6Ph6'/Ph, 6Th6'/Th, 6Ph7'/Th, and 6Th7'/Ph, respectively—are also listed in Table 1. The material with the introduction of halogen atoms, 7Br7'/Br, exhibited a deep-lying LUMO energy level and a slight red shift in its maximum absorption bands compared with the IID. The LUMO energy levels of materials based on the IID analogs were determined using electron-absorbing groups, which were all around -3.05 eV for this family of materials. Nevertheless, the HOMO energy levels of the materials in this series were altered accordingly. The introduction of different substituents at the 7,7' position induced a change in the HOMO's energy levels, which were more pronounced when comparing the energy levels of 6Ph6'/Ph with 6Th6'/Th or 5Ph5'/Ph with 5Th5'/Th and roughly exceeded 0.1 eV. In fact, the introduction of the $-Ph$ unit with the $-Th$ unit on each side of the IID (6Ph7'/Th vs. 6Th7'/Ph) resulted in a completely different HOMO energy level.

On the other hand, a comparison of 6Ph6'Ph with 5Ph5'Ph showed that both exhibited similar HOMO energy levels, suggesting that the change in the conjugation pattern induced by varying the position of the substituent did not lead to a substantial change in HOMO energy levels. The ϵ and f_{osc} of cross-conjugated materials were within the regions of 10,000 and 0.1, respectively, whereas the ϵ and f_{osc} of the linearly conjugated IID were far greater than those of the cross-conjugated material, approaching 30,000 and 0.5, respectively. The different positions of the electron-donating groups did not induce a strong effect on HOMO energy levels, which were more sensitive to changes in the substituent types. There was a pronounced correlation between the different conjugation modes and the absorption coefficient and oscillator strengths of the materials.

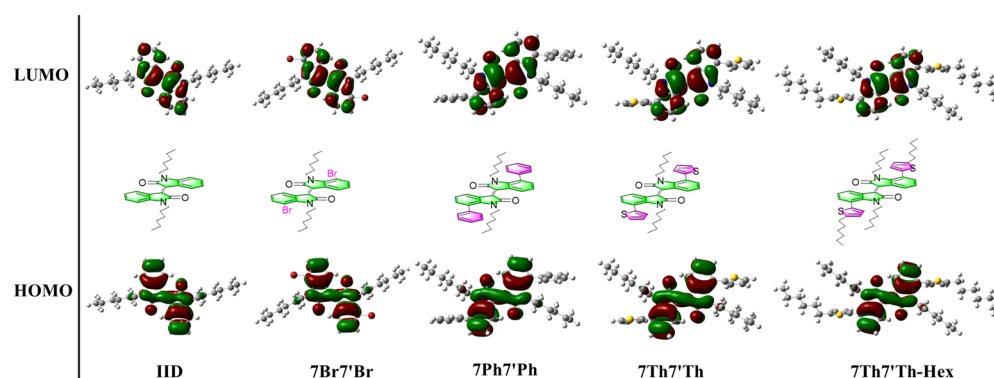


Figure 3. Optimized molecular geometries and frontier molecular orbitals of IID derivatives.

Table 1. Theoretically calculated values of oscillator strengths and frontier orbital energy levels.

	ϵ ($\text{cm}^{-1} \text{M}^{-1}$)	HOMO (eV)	LUMO (eV)	f_{osc}	ΔE_c (eV)
IID	16,387	−5.87	−3.01	0.11	2.86
7Br7'Br	12,278	−6.10	−3.29	0.11	2.81
7Ph7'Ph	16,104	−5.86	−3.06	0.15	2.80
7Th7'Th	14,827	−5.93	−3.09	0.14	2.84
7Th7'Th-Hex	15,699	−5.90	−3.08	0.13	2.82
5Ph5'Ph	3830	−5.74	−3.06	0.04	2.68
5Th5'Th	3900	−5.62	−3.10	0.07	2.52
6Ph6'Ph	28,656	−5.71	−3.06	0.48	2.65
6Th6'Th	32,976	−5.54	−3.10	0.77	2.44
6Ph7'Th	15,154	−5.80	−3.08	0.31	2.72
6Th7'Ph	20,351	−5.67	−3.08	0.43	2.59

The theoretical calculation of the torsion angle agreed with the crystallographic results of **7** (Figure 4). When the phenyl ring was presented as a substituent in **7**, the lowest energy was observed at dihedral angles of 60° to 80° , which was mainly related to the C–H $\cdots\pi$ interaction forces present within the molecule. The interatomic distance of C–H $\cdots\pi$ was calculated to be 2.96 Å. If the dihedral angle approached 0° , the C–H on the alkyl chain was hindered by the intermolecular space due to its proximity to the C–H of the aromatic moiety, resulting in elevated energy and instability.

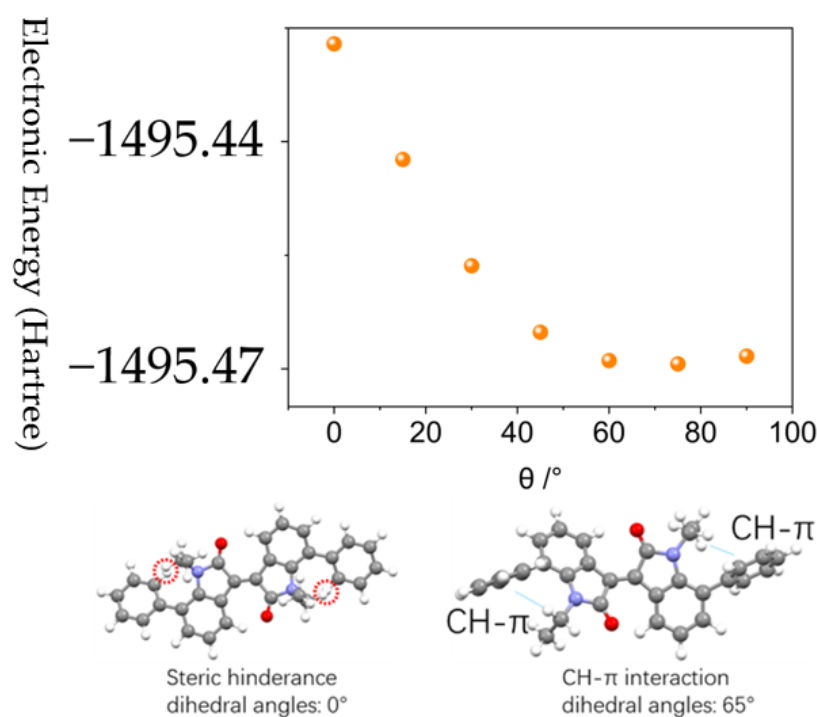


Figure 4. The theoretical calculation of the torsion angle of compound 7.

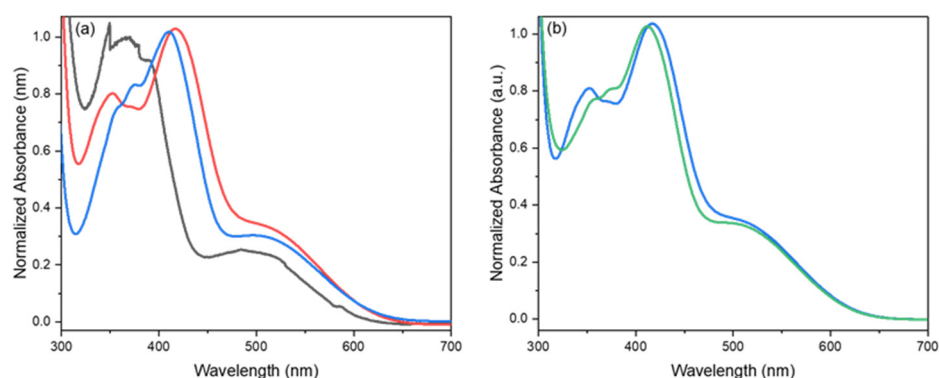
3.4. Optical Properties

The photophysical properties of the 7,7' IID derivatives were investigated using UV–Vis spectroscopy. The absorption spectra were recorded in a dilute tetrahydrofuran solution, and the corresponding absorption data of these materials are summarized in Table 2. All investigated materials exhibited broad absorption spectra in the visible spectral region with two distinct absorption bands in the regions of 330–450 nm and 470–650 nm. The peak in the high-energy area (330–450 nm) was caused by the π – π^* transition of the donor segments (phenyl/thienyl), and the peak in the low-energy area (470–650 nm) was associated with the intramolecular charge transfer transition. Compared with the IID, the introduction of the donor group resulted in a significant redshift of approximately 50 nm for both absorption bands. The corresponding bandgap decreased from 2.04 eV to 1.88 eV. A bathochromic shift of the low energy absorption peak was observed when the strength of the donor was increased. Approximately 15–25 nm was observed with respect to the bathochromic shift of the low energy absorption of **8** with the thienyl donor compared with that of the weaker donor phenyl unit (Figure 5a). The high-energy absorption bands were less affected by the substitution. The absorption spectra of **8** and **9** revealed almost identical absorptions in the visible range, indicating that the variation of alkyl groups on the thiophene virtually did not introduce effects on the electronic structure of this series of 7,7' IID derivatives (Figure 5b). These results are comparable to those of the derivatives substituted at the 5,5' or 6,6' positions, which exhibited two absorption bands, and their absorption ranges were also extremely close [16]. The optical bandgap of **9** was 1.89 eV, which was close to the optical bandgap of the 5Th5'Th and 6Th6'Th IID derivatives [24]. The 6,6' substitution on the IID core led to a stronger intramolecular charge transfer band due to the strong electronic coupling between the 6,6' substitution and the core. Neither the absorption band nor the optical bandgap of the material was significantly affected by differences in substitution patterns. On the other hand, the different positions of the substituent groups had an obvious effect on the absorption coefficient, which indicated that the ϵ of the linearly conjugated materials was more than four times higher than those of cross-conjugated materials.

Table 2. Optical characteristics of 7,7' IID derivatives.

	Low Energy	High Energy	ϵ ($\text{cm}^{-1} \text{M}^{-1}$) ^a	λ_{onset} (nm) ^a	$E_{\text{g}}^{\text{opt}}$ (eV) ^b
	$\lambda_{\text{max}} \text{ soln}$ (nm) ^a	$\lambda_{\text{max}} \text{ soln}$ (nm) ^a			
IID	484	365	1515	608	2.04
7Ph7'Ph	505	408	5100	636	1.95
7Th7'Th	528	411	4600	655	1.89
7Th7'Th-Hex	530	415	4700	660	1.88
5Th5'Th	518	420	3500	665	1.86
6Th6'Th	533	410	20,000	682	1.81

^a In tetrahydrofuran. ^b $E_{\text{g}}^{\text{opt}} = 1240/\lambda_{\text{onset}}$: the optical bandgap estimated from the absorption's onset in the tetrahydrofuran solution.

**Figure 5.** (a) UV-Vis spectra of IID (black), 8 (red), and 7 (blue); (b) 9 (blue) and 8 (green).

3.5. Electrochemical Properties

The redox properties of the synthesized molecules IID derivatives were studied using cyclic voltammetry (CV). CV experiments were performed in a dry dichloromethane solution comprising compounds (~5 mM) and TBAPF₆ as a supporting electrolyte using a three-electrode system: glassy carbon electrode as a working electrode, Pt electrode as the counter electrode, and Ag/Ag⁺ as a reference electrode. All molecules exhibited irreversible oxidation and two well-reversible reduction processes comprising the oxidation of the donor unit and the reduction of the IID unit (Figure 6). All compounds revealed stronger oxidative peaks than their reductive peaks. The oxidation onset potential measured using CVs was utilized to calculate HOMO levels, and the reduction onset potential was used to calculate the LUMO of the synthesized molecules. The introduction of the phenyl substituent into the IID scaffold increased the HOMO levels by 0.06 eV, while the energy level of the LUMO did not change significantly. The incorporation of thiophene was found to have the most important effect on the HOMO energy level, which was further increased to 5.62 eV with the employment of the thiophene substituent. The 7,7' IID derivatives exhibited a low-lying LUMO energy level (3.65 eV), with little change in energy levels due to variation in donor strength. By contrast, the HOMO energy level was variable and strongly depended on the electron donor's strength (Table 3). 7Th7'Th-Hex exhibited an electrochemical gap of 1.88 eV, which was 0.1 eV lower than the energy gap of IID, and this was mainly due to variations in the HOMO energy levels of material derivatives.

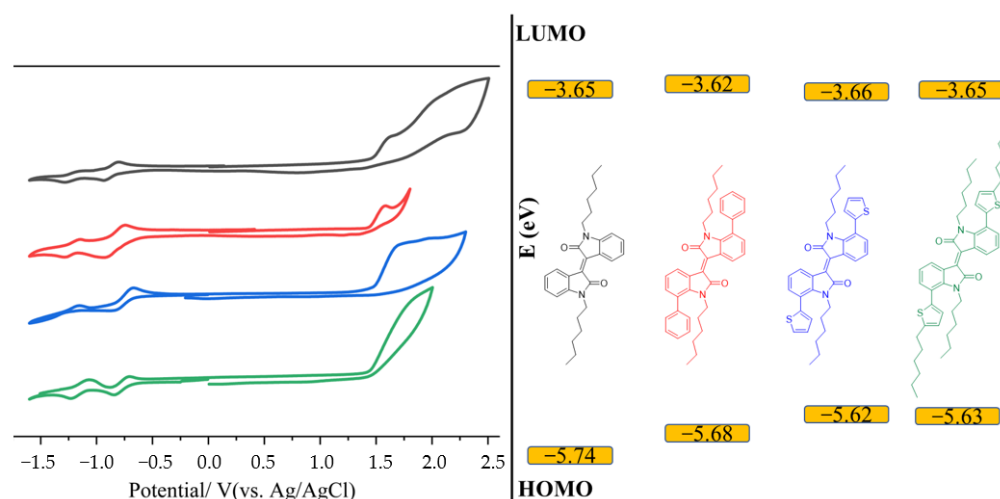


Figure 6. Cyclic voltammograms (left) and energy band diagram (right) of IID derivatives: IID (black), 7Ph7'Ph (red), 7Th7'Th (blue), and 7Th7'Th-Hex (green) in dichloromethane.

Table 3. Electrochemical characteristics of 7,7' IID derivatives.

	$E_{\text{ox}}^{\text{onset}}$ (V)	HOMO (eV) ^c	E_{red} (V)	$E_{\text{red}}^{\text{onset}}$ (V)	LUMO (eV) ^d	E_{g}^{cv} (eV) ^e
IID	1.47	−5.74	−0.96	−0.62	−3.65	2.09
7Ph7'Ph	1.41	−5.68	−0.87	−0.64	−3.62	2.06
7Th7'Th	1.35	−5.62	−0.84	−0.61	−3.66	1.96
7Th7'Th-Hex	1.36	−5.63	−0.85	−0.62	−3.65	1.98

^c $E_{\text{HOMO}} = -4.80 \text{ eV} - [(E_{\text{ox}}^{\text{onset}}) - E_{1/2}(\text{ferrocene})]$; ^d $E_{\text{LUMO}} = -4.80 \text{ eV} - [(E_{\text{red}}^{\text{onset}}) - E_{1/2}(\text{ferrocene})]$; ^e E_{g}^{cv} = electrochemical energy gap.

3.6. Electrical Characterization and Photovoltaic Devices

To demonstrate the utility of these cross-conjugated materials, we evaluated their potential as an electron transport layer in perovskite solar cells. A first electrical characterization was performed to probe their ability to transport charges. To assess their inherent charge transport properties, the electron mobility of 7,7' IID **8** was investigated by means of the space charge limited current (SCLC) method and compared with that reported in the literature (Figure 7a). The charge carrier mobility can be extracted using the Mott–Gurney equation:

$$J_{\text{SCLC}} = \frac{9}{8} \frac{\epsilon_0 \epsilon_r}{L^3} \mu V^2 \quad (1)$$

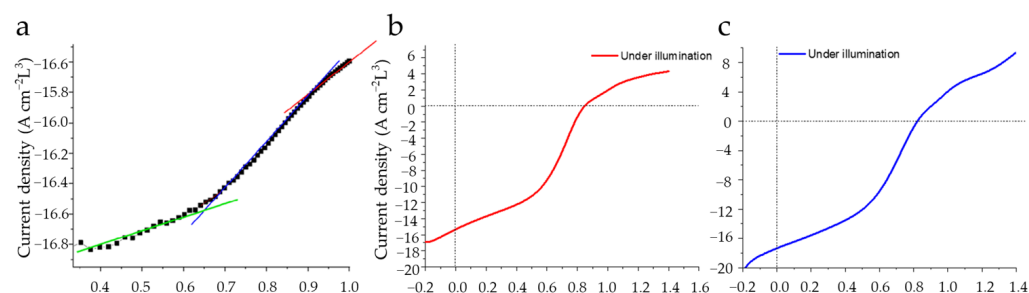


Figure 7. (a) SCLC measurement of the electron-only device for 7Th7'Th; J – V curves for the best-performing devices. (b) 7Ph7'Ph (red); (c) 7Th7'Th (blue).

Therein, ϵ_0 is the permittivity of vacuum, ϵ_r is the relative permittivity of the organic compound, μ is the charge carrier mobility, V is the voltage, and L is the thickness of

the tested layer. The estimated electron mobility is $5.23 \times 10^{-6} \text{ cm}^2 \text{ V}^{-1} \text{ s}^{-1}$, which is more than two orders of magnitude lower than that of 1-(3-methyloxycarbonyl) propyl (1-phenyl [6,6]) C61 (PCBM, $\mu_{\text{PCBM}} = 1.22 \times 10^{-3} \text{ cm}^2 \text{ V}^{-1} \text{ s}^{-1}$) [25].

The devices were manufactured using the following structure: FTO/TiO₂/TiO₂ mesoporous/perovskite /TBABr/7,7' IID-7 or 8 /Au. Figure 7b,c show the current density–voltage (*J*–*V*) curves measured under illumination using the optimized devices of 7 and 8. The 7-based devices achieved a good power conversion efficiency (PCE) of 5.70% with an open-circuit voltage (*V*_{oc}) of 0.84 V, a short-circuit current density (*J*_{sc}) of 15.31 mA cm^{−2}, and a fill factor (FF) of 43.09%. A PCE of >6% was improved by increasing *J*_{sc} without sacrificing *V*_{oc}, and FF was achieved in the 8-based device (Table 4). The average PCEs throughout the four cells were 4.53% and 5.13%. The optical properties of the perovskite layer are shown in Figures S3 and S4.

Table 4. Photovoltaic parameters of the device’s performances.

Materials	PCE (%)	<i>V</i> _{oc} (V)	<i>J</i> _{sc} (mA/cm ²)	FF (%)
7	5.70	0.84	15.31	43.09
8	6.07	0.82	17.34	42.06
P3HT	8.14	0.85	15.73	60.00

In addition to the lower mobility limiting the PCE performance, we performed control experiments based on poly(3-hexylthiophene) (P3HT) to explore the reasons. Our optimal control device using P3HT as the hole transport layer showed a PCE value of 8.14%, which was lower than what is reported in the literature (Table 4) [26]. One of the explanations for the lower PCEs values in our devices might be related to the non-radiative recombination, which was caused by the structural and morphological quality of the photoactive layer. It is generally accepted that the non-radiative recombination losses arise from defects (charge carrier traps) either in the bulk perovskite or at the interfaces. Therefore, an optimization effort to passivate the defects on the perovskite surfaces and at the grain boundaries is necessary to enhance efficiency.

4. Conclusions

In summary, cross-conjugated IID materials are less developed because they are generally considered to result in poor orbital overlap, less electron delocalization, and poor intermolecular couplings. The successful synthesis of three new series of 7,7'-difunctionalized IID compounds with different electron donor groups enabled a systematic study of the electron structure–property relationships of this class of materials. Our study showed that the optical and electrochemical properties of these materials can be modulated by peripheral substituents. The introduction of stronger donor moieties than phenyl (e.g., thiophene or hexyl-thiophene) led to a significant redshift in absorption. The 7,7' IID-based molecule exhibited a low-lying LUMO energy level and little change in energy level due to variations in donor strength. By contrast, the HOMO energy level was variable and depended on the electron donor’s strength with respect to the donor moiety. The frontline orbital energy was more influenced by the type of substituent, while the different positions of the substituents resulted in sharp fluctuations with respect to oscillator strength, with cross-conjugated materials exhibiting low oscillator strengths and absorption coefficients. The cross material displayed a moderate PCE as an electron transport layer material in the working device. This suggests that cross-conjugated systems are useful materials for optoelectronic devices, as this substitution leads to the spatial isolation of frontier molecular orbitals.

Supplementary Materials: The following supporting information can be downloaded at <https://www.mdpi.com/article/10.3390/electronics12153313/s1>. Figure S1: The crystal structure of 7Ph7/Ph; Figure S2: The crystal structure of 7Br7/Br; Figure S3: SEM image of perovskite solar cell based on 7Ph7/Ph; Figure S4: SEM image of perovskite solar cell based on 7Br7/Br; Figure S5: ^1H NMR spectra of compound 7; Figure S6: ^{13}C NMR spectra of compound 7; Figure S7: ^1H NMR spectra of compound 8; Figure S8: ^{13}C NMR spectra of compound 8; Figure S9: ^1H NMR spectra of compound 9; Figure S10: ^{13}C NMR spectra of compound 9.

Author Contributions: Conceptualization, A.Y.; methodology, S.R.; software, Y.W.; validation, S.R. and A.Y.; formal analysis, S.R. and A.H.; investigation, S.R. and A.H.; resources, A.Y.; data curation, S.R.; writing—original draft preparation, S.R.; writing—review and editing, A.Y.; visualization, S.R.; supervision, A.Y.; project administration, A.Y.; funding acquisition, A.Y. All authors have read and agreed to the published version of the manuscript.

Funding: This research was funded by ANR-16-CE07-0024 (GATE) from the French state managed by the National Research Agency under the Investments for the Future program. S.R. thanks the China Scholarship Council for a Ph.D. fellowship (No. 201808070090) and the fellowship of the China Postdoctoral Science Foundation (No. 2022TQ0399).

Data Availability Statement: Not applicable.

Acknowledgments: Part of the work was carried out by an intern from Ecole Polytechnique in Paris; we thank the University of Saclay for offering this internship in molecular chemistry.

Conflicts of Interest: The authors declare no conflict of interest.

References

1. Zhang, W.; Shi, K.; Lai, J.; Zhou, Y.; Wei, X.; Che, Q.; Wei, J.; Wang, L.; Yu, G. Record-High Electron Mobility Exceeding $16\text{ cm}^2\text{ V}^{-1}\text{ s}^{-1}$ in Bisoindigo-Based Polymer Semiconductor with a Fully Locked Conjugated Backbone. *Adv. Mater.* **2023**, *35*, e2300145. [[CrossRef](#)]
2. Li, J.-L.; Cao, J.-J.; Duan, L.-L.; Zhang, H.-L. Evolution of Isoindigo-Based Electron-Deficient Units for Organic Electronics: From Natural Dyes to Organic Semiconductors. *Asian J. Org. Chem.* **2018**, *7*, 2147–2160. [[CrossRef](#)]
3. Wei, X.; Zhang, W.; Yu, G. Semiconducting Polymers Based on Isoindigo and Its Derivatives: Synthetic Tactics, Structural Modifications, and Applications. *Adv. Funct. Mater.* **2021**, *31*, 2010979. [[CrossRef](#)]
4. Jung, J.W. A low band gap conjugated small molecule based on isoindigo flanked with diketopyrrolopyrrole for efficient organic solar cells. *Dye. Pigment.* **2017**, *137*, 512–517. [[CrossRef](#)]
5. Zhu, M.; Guo, Y.; Liu, Y. A thriving decade: Rational design, green synthesis, and cutting-edge applications of isoindigo-based conjugated polymers in organic field-effect transistors. *Sci. China Chem.* **2022**, *65*, 1225–1264. [[CrossRef](#)]
6. Ngai, J.H.L.; Polena, J.; Afzal, D.; Gao, X.; Kapadia, M.; Li, Y. Green Solvent-Processed Hemi-Isoindigo Polymers for Stable Temperature Sensors. *Adv. Funct. Mater.* **2022**, *32*, 2110995. [[CrossRef](#)]
7. Parr, Z.S.; Borges-Gonzalez, J.; Rashid, R.B.; Thorley, K.J.; Meli, D.; Paulsen, B.D.; Strzalka, J.; Rivnay, J.; Nielsen, C.B. From p- to n-Type Mixed Conduction in Isoindigo-Based Polymers through Molecular Design. *Adv. Mater.* **2022**, *34*, e2107829. [[CrossRef](#)] [[PubMed](#)]
8. Li, W.; Du, C.Z.; Chen, X.Y.; Fu, L.; Gao, R.R.; Yao, Z.F.; Wang, J.Y.; Hu, W.; Pei, J.; Wang, X.Y. BN-Anthracene for High-Mobility Organic Optoelectronic Materials through Periphery Engineering. *Angew. Chem. Int. Ed. Engl.* **2022**, *61*, e202201464. [[CrossRef](#)]
9. Ren, S.; Habibi, A.; Ni, P.; Nahdi, H.; Bouanis, F.Z.; Bourcier, S.; Clavier, G.; Frigoli, M.; Yassar, A. Synthesis and characterization of solution-processed indophenine derivatives for function as a hole transport layer for perovskite solar cells. *Dye. Pigment.* **2023**, *213*, 111136. [[CrossRef](#)]
10. Lei, T.; Wang, J.Y.; Pei, J. Design, synthesis, and structure-property relationships of isoindigo-based conjugated polymers. *Acc. Chem. Res.* **2014**, *47*, 1117–1126. [[CrossRef](#)]
11. Ren, S.; Yassar, A. Recent Research Progress in Indophenine-Based-Functional Materials: Design, Synthesis, and Optoelectronic Applications. *Materials* **2023**, *16*, 2474. [[CrossRef](#)] [[PubMed](#)]
12. Randell, N.M.; Kelly, T.L. Recent Advances in Isoindigo-Inspired Organic Semiconductors. *Chem. Rec.* **2019**, *19*, 973–988. [[CrossRef](#)] [[PubMed](#)]
13. Park, S.; Ha, J.; Khan, M.F.; Im, C.; Park, J.Y.; Yoo, S.H.; Rehman, M.A.; Kang, K.; Lee, S.H.; Jun, S.C. Pronounced Optoelectronic Effect in n–n ReS₂ Homostructure. *ACS Appl. Electron. Mater.* **2022**, *4*, 4306–4315. [[CrossRef](#)]
14. Rabeel, M.; Javed, S.; Khan, R.; Akram, M.A.; Rehman, S.; Kim, D.K.; Khan, M.F. Controlling the Wettability of ZnO Thin Films by Spray Pyrolysis for Photocatalytic Applications. *Materials* **2022**, *15*, 3364. [[CrossRef](#)] [[PubMed](#)]
15. Maqsood, M.F.; Raza, M.A.; Rehman, Z.U.; Tayyeb, A.; Makhdoom, M.A.; Ghafoor, F.; Latif, U.; Khan, M.F. Role of Solvent Used in Development of Graphene Oxide Coating on AZ31B Magnesium Alloy: Corrosion Behavior and Biocompatibility Analysis. *Nanomaterials* **2022**, *12*, 3745. [[CrossRef](#)]

16. Estrada, L.A.; Stalder, R.; Abboud, K.A.; Risko, C.; Brédas, J.-L.; Reynolds, J.R. Understanding the Electronic Structure of Isoindigo in Conjugated Systems: A Combined Theoretical and Experimental Approach. *Macromolecules* **2013**, *46*, 8832–8844. [[CrossRef](#)]
17. Deng, P.; Zhang, Q. Recent developments on isoindigo-based conjugated polymers. *Polym. Chem.* **2014**, *5*, 3298–3305. [[CrossRef](#)]
18. Ganguly, A.; Zhu, J.; Kelly, T.L. Effect of Cross-Conjugation on Derivatives of Benzoisoindigo, an Isoindigo Analogue with an Extended π -System. *J. Phys. Chem. C* **2017**, *121*, 9110–9119. [[CrossRef](#)]
19. Yao, H.; Ye, L.; Hou, J.; Jang, B.; Han, G.; Cui, Y.; Su, G.M.; Wang, C.; Gao, B.; Yu, R.; et al. Achieving Highly Efficient Nonfullerene Organic Solar Cells with Improved Intermolecular Interaction and Open-Circuit Voltage. *Adv. Mater.* **2017**, *29*, 1700254. [[CrossRef](#)]
20. Becke, A.D. Density-functional thermochemistry. III. The role of exact exchange. *J. Chem. Phys.* **1993**, *98*, 5648–5652. [[CrossRef](#)]
21. Lee, C.; Yang, W.; Parr, R.G. Development of the Colle-Salvetti correlation-energy formula into a functional of the electron density. *Phys. Rev. B Condens. Matter* **1988**, *37*, 785–789. [[CrossRef](#)]
22. Miehlich, B.; Savin, A.; Stoll, H.; Preuss, H. Results obtained with the correlation energy density functionals of Becke and Lee, Yang and Parr. *Chem. Phys. Lett.* **1989**, *157*, 200–206. [[CrossRef](#)]
23. Frisch, M.J.; Trucks, G.W.; Schlegel, H.B.; Scuseria, G.E.; Robb, M.A.; Cheeseman, J.R.; Scalmani, G.; Barone, V.; Petersson, G.A.; Nakatsuji, H.; et al. *Gaussian 16 Rev. C.01*; Gaussian: Wallingford, CT, USA, 2016.
24. Elsayy, W.; Lee, C.L.; Cho, S.; Oh, S.H.; Moon, S.H.; Elbarbary, A.; Lee, J.S. Isoindigo-based small molecules for high-performance solution-processed organic photovoltaic devices: The electron donating effect of the donor group on photo-physical properties and device performance. *Phys. Chem. Chem. Phys.* **2013**, *15*, 15193–15203. [[CrossRef](#)] [[PubMed](#)]
25. Perez, G.S.; Dasgupta, S.; Żuraw, W.; Pineda, R.F.; Wojciechowski, K.; Jagadamma, L.K.; Samuel, I.; Robertson, N. Solution-processable perylene diimide-based electron transport materials as non-fullerene alternatives for inverted perovskite solar cells. *J. Mater. Chem. A* **2022**, *10*, 11046–11053. [[CrossRef](#)]
26. Jung, E.H.; Jeon, N.J.; Park, E.Y.; Moon, C.S.; Shin, T.J.; Yang, T.Y.; Noh, J.H.; Seo, J. Efficient, stable and scalable perovskite solar cells using poly(3-hexylthiophene). *Nature* **2019**, *567*, 511–515. [[CrossRef](#)] [[PubMed](#)]

Disclaimer/Publisher's Note: The statements, opinions and data contained in all publications are solely those of the individual author(s) and contributor(s) and not of MDPI and/or the editor(s). MDPI and/or the editor(s) disclaim responsibility for any injury to people or property resulting from any ideas, methods, instructions or products referred to in the content.